Research Article Vol. 43, No. 10 / October 2026 / Journal of the Optical Society of America B C41

Journal of the Optical Society of America B

OPTICAL PHYSICS

Orbital angular momentum control of third-harmonic generation and vortex dichroism in isotropic media [Invited]

Szymon Krukowski[1] and Kayn A. Forbes[2,*]

[1]School of Engineering, Mathematics and Physics, University of East Anglia, Norwich Research Park, Norwich NR4 7TJ, UK
[2]School of Chemistry, University of East Anglia, Norwich Research Park, Norwich NR4 7TJ, UK
*k.forbes@uea.ac.uk

Received 27 March 2026; revised 14 May 2026; accepted 26 May 2026; posted 26 May 2026; published 2 July 2026

Structured light carrying orbital angular momentum enables new regimes of nonlinear light–matter interaction. Here, we develop a molecular quantum electrodynamics description of third-harmonic generation (THG) driven by focused Laguerre–Gaussian beams in isotropic molecular media. We show that the nonparaxial longitudinal field components of a tightly focused beam permit THG with circularly polarized excitation in an isotropic fluid, a process forbidden for plane waves and paraxial beams. Within the electric-dipole approximation, the resulting emission is achiral, although for circularly polarized excitation its spatial structure depends on the relative sign of $\sigma\ell$ through nonparaxial spin–orbit coupling. Including electric–magnetic dipole interference introduces a chiral contribution to the nonlinear response, giving rise to third-harmonic vortex dichroism (THVD). The emitted intensity then acquires a component linear in the topological charge ℓ, reversing sign with either the wavefront handedness or molecular chirality. Numerical modeling reveals corresponding spatial asymmetries in the harmonic field. These results establish both an allowed pathway for circularly polarized THG in isotropic fluids and the first, to our knowledge, chiroptical analog of THG in such media, identifying orbital angular momentum as a new control parameter for nonlinear chiral spectroscopy.

https://doi.org/10.1364/JOSAB.600313

1. INTRODUCTION

Nonlinear optics studies the interaction of intense electromagnetic fields with matter, where the induced material response becomes nonlinear in the applied optical field [1–3]. Such effects typically arise at the high field strengths produced by lasers and give rise to a wide range of phenomena, including harmonic generation, wave mixing, and nonlinear scattering processes [3,4]. These interactions form the basis of many modern spectroscopic and imaging techniques [5–10], and continue to provide new opportunities for controlling light–matter interactions [11,12].

In recent years, there has been increasing interest in the role of the spatial structure of light in nonlinear optical processes [13–15]. Structured light fields, whose amplitude, phase, and polarization distributions are deliberately engineered [16,17], provide additional degrees of freedom for tailoring optical interactions. Of particular relevance in this work are optical vortex beams, which possess a helical phase structure of the form $\exp(i\ell\phi)$ and carry $\ell\hbar$ units of orbital angular momentum (OAM) per photon [18]. The unique properties of these beams have led to numerous applications in optical manipulation, communication, and quantum optics [19].

A molecule is said to be chiral if it cannot be superposed onto its mirror image by any combination of rotations and translations, and chirality plays a central role throughout chemistry. Chiral molecules therefore exist as pairs of enantiomers with identical chemical composition but opposite handedness. These enantiomers can interact differently with other chiral systems, leading to discriminatory behavior in chemical reactions and molecular interactions [4,20–22]. This selectivity underpins much of biochemistry and drug efficacy, making the assignment of absolute handedness a critical capability in health and pharmaceutical applications.

Light may also be chiral, its handedness arising from both its polarization and spatial phase structure [23,24]. Optical activity arises when such chiral molecules interact differently with left- and right-handed light, a phenomenon that underpins chiroptical spectroscopy and enables the determination of absolute molecular configuration [25,26]. The vast majority of such techniques rely on the chirality associated with circularly polarized states of light.

The topological charge ℓ of a vortex beam not only determines its OAM but, as a pseudoscalar, also defines the handedness of its wavefront. This introduces a distinct form

of optical chirality associated with the sign of ℓ. Unlike the bounded polarization helicity $\sigma \in [-1, 1]$, the wavefront helicity $\ell \in \mathbb{Z}$ is unbounded, offering new routes to enhanced chiral interactions. Consequently, interactions between twisted light and chiral matter have attracted considerable interest. In particular, vortex dichroism describes a differential optical response to light carrying opposite signs of orbital angular momentum [23,24]. Such effects arise from the coupling between the handedness of the optical wavefront and the intrinsic chirality of matter.

Despite growing interest in structured light, the role of orbital angular momentum in nonlinear chiroptical processes remains largely unexplored [23,24,27–29]. In particular, third-harmonic generation (THG) in isotropic molecular media is typically forbidden for circularly polarized excitation within the electric-dipole approximation [3], and no direct third-harmonic analog of vortex dichroism has previously been established.

In this work, we investigate nonlinear interactions of focused optical vortex beams in isotropic molecular media. Within a molecular quantum electrodynamics framework, we show that third-harmonic generation with a circularly polarized input is not forbidden. We then introduce a new nonlinear chiroptical effect, third-harmonic vortex dichroism (THVD), and demonstrate how the handedness of optical vortices gives rise to chiral-sensitive nonlinear optical signals through the spatial structure of the generated fields, establishing a new route to nonlinear chiral spectroscopy.

2. THIRD-HARMONIC GENERATION WITH LAGUERRE–GAUSSIAN MODES

In the theory of molecular quantum electrodynamics (MQED) [4], the interaction Hamiltonian for the dipole coupling of some molecule ξ with a radiation field can be written as

$$H_{\mathrm{int}}(\xi) = -\boldsymbol{\mu}(\xi)\cdot\mathbf{E}(\mathbf{R}_\xi) - \mathbf{m}(\xi)\cdot\mathbf{B}(\mathbf{R}_\xi), \tag{1}$$

where $\boldsymbol{\mu}(\xi)$ and $\mathbf{m}(\xi)$ are the electric and magnetic dipole moment operators, and $\mathbf{R}_\xi$ is the position vector of ξ. The electric and magnetic field operator mode expansions for a Laguerre–Gaussian (LG) beam propagating in the z direction, in cylindrical coordinates (r, ϕ, z), can be expressed as [30]

$$\mathbf{E}_{\mathrm{LG}}(\mathbf{r}) = \sum_{k,\ell,p} \Omega\Bigg[\Bigg(\alpha\hat{\mathbf{x}} + \beta\hat{\mathbf{y}} + \hat{\mathbf{z}}\frac{i}{k}\Bigg\{\alpha\Bigg(\gamma\cos\phi - \frac{i\ell}{r}\sin\phi\Bigg) + \beta\Bigg(\gamma\sin\phi + \frac{i\ell}{r}\cos\phi\Bigg)\Bigg\}\Bigg) \times f_{\mathrm{LG}}\, a_{\ell,p}\, \mathrm{e}^{i(kz+\ell\phi)} - \mathrm{H.c}\Bigg], \tag{2}$$

$$\mathbf{B}_{\mathrm{LG}}(\mathbf{r}) = \sum_{k,\ell,p} \frac{\Omega}{c}\Bigg[\Bigg(\alpha\hat{\mathbf{y}} - \beta\hat{\mathbf{x}} + \hat{\mathbf{z}}\frac{i}{k}\Bigg\{\alpha\Bigg(\gamma\sin\phi + \frac{i\ell}{r}\cos\phi\Bigg) - \beta\Bigg(\gamma\cos\phi - \frac{i\ell}{r}\sin\phi\Bigg)\Bigg\}\Bigg) \times f_{\mathrm{LG}}\, a_{\ell,p}\, \mathrm{e}^{i(kz+\ell\phi)} - \mathrm{H.c}\Bigg], \tag{3}$$

where $\mathbf{r}$ is a position vector; k is the wavenumber; ℓ is the previously mentioned topological charge, where $\ell \in \mathbb{Z}$; p is the radial index, where $p \in \mathbb{N}$; $\Omega = i\left(\frac{\hbar c k}{2\varepsilon_0 V A^2_{|\ell|,p}}\right)^{\frac{1}{2}}$ is a normalization constant; i is the imaginary unit; $\hbar$ is the reduced Planck's constant; c is the speed of light; ε_0 is the vacuum permittivity; V is the quantization volume; $A_{|\ell|,p}$ is a constant that ensures correct energy normalization of the LG mode, including both transverse and longitudinal field components [30]; α and β are the complex Jones vector coefficients specifying the input transverse polarization state, with $|\alpha|^2 + |\beta|^2 = 1$; $\gamma = \frac{|\ell|}{r} - \frac{2r}{w[z]^2} + \frac{ikr}{R[z]} - \frac{4r}{w[z]^2}\frac{L_{p-1}^{|\ell|+1}}{L_p^{|\ell|}}$ [24,31] (for $p = 0$, the term involving $L_{p-1}^{|\ell|+1}$ is understood to vanish), where $w[z]$ denotes the beam width at some distance z; $R[z]$ is the radius of curvature of the beam's wavefronts at z; $L_p^{|\ell|}$ is the generalized Laguerre polynomial; ϕ is the azimuthal angle around the beam profile; f_{LG} is the radial distribution function of the LG modes for some value of z, given by [18]

$$f_{\mathrm{LG}} = \sqrt{\frac{2p!}{\pi w_0^2 (p+|\ell|)!}}\frac{w_0}{w[z]}\left(\frac{\sqrt{2}r}{w[z]}\right)^{|\ell|} L_p^{|\ell|}\left[\frac{2r^2}{w^2[z]}\right] \times \mathrm{e}^{-\frac{r^2}{w^2[z]}}\mathrm{e}^{i\left(\frac{kr^2}{2R[z]} - (2p+|\ell|+1)\zeta[z]\right)}, \tag{4}$$

where w_0 is the beam waist; $\zeta[z]$ is the Gouy phase; $a_{\ell,p}$ is the annihilation operator; and H.c. is the associated Hermitian conjugate, representing the terms associated with the raising operator $a^\dagger_{\ell,p}$. The full local polarization structure is contained in the complete vector fields in Eqs. (2) and (3); α and β specify the input transverse Jones state, while the spatial vortex structure and the accompanying longitudinal components are carried by f_{LG}, $\exp(i\ell\phi)$, and the transversality corrections.

The $\hat{\mathbf{x}}$- and $\hat{\mathbf{y}}$-dependent terms in Eqs. [(2)–(3)] represent the 2D polarization state of the electric and magnetic fields. This transverse property of light (with respect to the direction of propagation, z) is well understood using paraxial models of light beams [32]. However, in order to satisfy Maxwell's equations, all real electromagnetic beams must contain longitudinal (nonparaxial) components. The magnitude of the $\hat{\mathbf{z}}$-dependent terms in Eqs. [(2)–(3)] increases with a tighter focus relative to the transverse components. The field expressions in Eqs. [(2)–(3)] should therefore be understood as analytic, Maxwell-consistent focused LG modes retaining the leading longitudinal components required by transversality. In this sense, "nonparaxial" refers to the inclusion of higher-order field components beyond the zeroth-order transverse paraxial field, following the standard

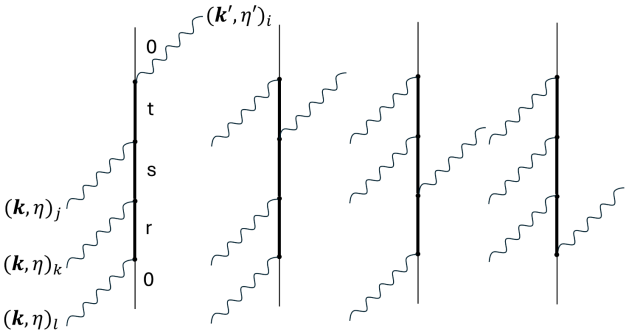

Fig. 1. Four topologically distinct time-ordered Feynman diagrams describing THG required in the sum over all pathways. Time flows vertically. The intermediate states are denoted as $|r\rangle$, $|s\rangle$, and $|t\rangle$. Each photon is labeled using Latin indices, i, j, k, and l; each also has an associated wave vector, $\mathbf{k}$, and polarization label, η.

Lax expansion terminology [24]. The transverse LG envelope supplies the usual paraxial mode structure, while the longitudinal field terms are the first beyond-paraxial corrections required for consistency with Maxwell's equations. These fields are not intended to represent the full vectorial focal field of a particular high-numerical-aperture lens system. In such cases, the detailed focal distribution depends on the focusing geometry and may be described using Richards–Wolf or angular-spectrum methods [33–35]. The purpose of the present field model is instead to isolate the longitudinal and spin–orbit terms that enter the molecular polarization contractions governing the THG and THVD source terms.

THG is a four-photon process in which three input photons of frequency ω are annihilated, and a single photon of frequency 3ω is created [4,36]. The topologically distinct Feynman (time-ordered) diagrams required to describe THG are shown in Fig. 1. The initial state of the light–molecule system may be written as a product wave function given by $|I\rangle = |n(\mathbf{k},\eta)\rangle \prod_\xi^N |E_0(\xi)\rangle$, where n is the occupation number of the incident beam, η designates the polarization state, $E_0(\xi)$ is the initial energy state of ξ, and N is the number of molecules.

Under the assumption of purely electric-dipole interactions [first term in Eq. (1)], THG is described by fourth-order time-dependent perturbation theory, involving three annihilation events at the fundamental frequency ω and one creation event at the harmonic frequency 3ω. The intermediate states R, S, and T are complete virtual states of the combined molecule–radiation system. Formally, each contains a molecular intermediate state together with the radiation state obtained after one, two, or three light–matter interaction events. Thus, the product of interaction Hamiltonians connects the initial state, containing n photons in the incident mode and all molecules in their ground states, to the final state, containing one emitted third-harmonic photon.

The action of the field operators in Eqs. (2)–(3) provides the photon number factor $\sqrt{n(n-1)(n-2)}$, the spatial mode functions, polarization vectors, and optical phase factors. The corresponding molecular transition moments and energy denominators from all time-ordered pathways are collected into the fourth-rank hyperpolarizability tensor β_{ijkl}. The resulting electric-dipole scattering amplitude is therefore

$$M_{FI} = \sum_{R,S,T} \frac{\langle F|H_{\rm int}|T\rangle\langle T|H_{\rm int}|S\rangle\langle S|H_{\rm int}|R\rangle\langle R|H_{\rm int}|I\rangle}{(E_I - E_R)(E_I - E_S)(E_I - E_T)}$$

$$= -\sqrt{3}\left(\frac{\hbar c k}{2\varepsilon_0 V}\right)^2 \sqrt{n(n-1)(n-2)}\, \bar{e}'_i e_j e_k e_l \times \sum_\xi \beta_{ijkl}(\xi)\, \overline{\tilde{f}'_{\rm LG}(r_\xi, z_\xi)}\, \tilde{f}^3_{\rm LG}(r_\xi, z_\xi)\, e^{i\Delta\Phi(r_\xi,\phi_\xi,z_\xi)}, \tag{5}$$

where the phase mismatch is

$$\Delta\Phi(r_\xi,\phi_\xi,z_\xi) = (3k-k')z_\xi + (3\ell-\ell')\phi_\xi + \frac{r_\xi^2}{2}\left(\frac{3k}{R(z_\xi)} - \frac{k'}{R'(z_\xi)}\right) - \big[3(2p+|\ell|+1)\zeta(z_\xi) - (2p'+|\ell'|+1)\zeta'(z_\xi)\big]. \tag{6}$$

Note that we separate the phase from the Laguerre–Gaussian mode function by writing

$$f_{\rm LG}(r,z) = \tilde{f}_{\rm LG}(r,z)\, \exp\left[i\left(\frac{kr^2}{2R[z]} - (2p+|\ell|+1)\zeta[z]\right)\right], \tag{7}$$

where $\tilde{f}_{\rm LG}$ denotes the LG mode with the Gouy and wavefront curvature phases removed.

In the case of linearly polarized input fields, the nonlinear azimuthal source phase is determined solely by the orbital contribution $3\ell\phi_\xi$. For a circularly polarized input, an additional spin-dependent contribution modifies the azimuthal phase, leading to a source phase of the form $e^{i(3\ell+2\sigma)\phi}$, and correspondingly altered phase-matching conditions. Both of these cases are considered explicitly in the following subsections. We employ Einstein summation notation throughout, with repeated indices implying summation. Here, e_i denotes the electric field polarization vector of photon i, and an overbar indicates complex conjugation. E_I represents the total energy of the system in its initial state. The spatial mode function for the emitted photon, $f'_{\rm LG}$, is defined using (4) with the substitution $k' \to 3k$, reflecting energy conservation in the third-harmonic process, while the azimuthal phase of the emitted mode is fixed by conservation of total angular momentum of the radiation field. For the linearly polarized case, energy and orbital-angular-momentum conservation imply $k' = 3k$ and $\ell' = 3\ell$, so that the longitudinal and azimuthal phase-matching conditions are satisfied. However, the Gouy phase introduces a mode-order-dependent axial mismatch away from the focal plane, limiting coherent buildup and reducing conversion efficiency. The fourth-rank hyperpolarizability tensor β_{ijkl} contains the molecular response terms; its general form is provided in Supplement 1. Here and throughout, Latin indices refer to laboratory-frame components, while Greek indices refer to molecular-frame components. For a homogeneous isotropic solution of identical molecules, the discrete sum over molecular centers may be replaced by a continuum integral with the

constant number density ρ_0, such that

$$\sum_{\xi} \beta_{ijkl}(\xi)\, \overline{\tilde{f}'_{\mathrm{LG}}(r_\xi, z_\xi)}\, \tilde{f}^3_{\mathrm{LG}}(r_\xi, z_\xi)\, e^{i\Delta\Phi(r_\xi,\phi_\xi,z_\xi)} \rightarrow \rho_0 \int_V d^3R\, \beta_{ijkl}(\mathbf{R})\, \overline{\tilde{f}'_{\mathrm{LG}}(\mathbf{R})}\, \tilde{f}^3_{\mathrm{LG}}(\mathbf{R})\, e^{i\Delta\Phi(\mathbf{R})}. \quad (8)$$

The THG rate follows from Fermi's golden rule,

$$\Gamma = \frac{2\pi}{\hbar}\rho_f\, |M_{FI}|^2, \quad (9)$$

where ρ_f is the density of final radiation states and M_{FI} is the total scattering amplitude for the molecular ensemble. The corresponding radiant intensity per unit solid angle follows as $I = \hbar c k' \frac{d\Gamma}{d\Omega}$, since the emitted harmonic photon carries energy $\hbar c k'$. Taking the final-state density for the emitted harmonic mode as $\rho_f = \frac{V k'^2 d\Omega}{(2\pi)^3 \hbar c}$, imposing $k' = 3k$ by energy conservation, using $\bar{I}_0 = \frac{\langle n\rangle \hbar k c^2}{V}$, and defining the third-order coherence function $g^{(3)} = \frac{\langle n(n-1)(n-2)\rangle}{\langle n\rangle^3}$, Eq. (5) gives the local third-harmonic source intensity:

$$I_{\mathrm{THG}} = \frac{81\bar{I}_0^3 g^{(3)} k^4 N_{\mathrm{eff}}^2}{64\pi^2 \varepsilon_0^4 c^2} \tilde{f}^6_{\mathrm{LG}} \tilde{f}'^2_{\mathrm{LG}} \left|\bar{e}'_i e_j e_k e_l \beta_{ijkl}\right|^2, \quad (10)$$

where N_{eff} denotes an effective number of molecules that contribute coherently within the local interaction region. Equation (10) is therefore a local coherent source intensity in the focal region, rather than a fully propagated third-harmonic output from an extended sample. No explicit focal length appears because the focusing dependence is encoded in the LG mode parameters and the vectorial field structure, including the longitudinal field components. For the isotropic fluid considered below, the orientational average is performed at the level of the coherent amplitude before forming the modulus square. This is because third-harmonic generation is a coherent process: the emitted fields from different molecules retain fixed phase relations, so amplitudes add prior to squaring and interference terms must be preserved.

Equation (10) gives the local coherent source intensity prior to orientational averaging, for molecules with fixed orientation relative to the optical vortex beam. The orientational average is performed only over molecular orientations; the transverse spatial structure of the vortex beam enters separately through the local field vectors, mode functions, longitudinal components, and phase factors evaluated at each molecular position. To account for randomly oriented molecules in an isotropic fluid, we perform a fourth-rank rotational average [4] using standard methods (see Supplement 1), yielding

$$I_{\mathrm{THG}} = \frac{81\bar{I}_0^3 g^{(3)} k^4 N_{\mathrm{eff}}^2}{1600\pi^2 \varepsilon_0^4 c^2} \tilde{f}^6_{\mathrm{LG}} \tilde{f}'^2_{\mathrm{LG}} |\mathbf{e}\cdot\mathbf{e}|^2 |\mathbf{e}\cdot\bar{\mathbf{e}}'|^2 |\beta_{\lambda\lambda\mu\mu}|^2. \quad (11)$$

The spatial intensity distribution is obtained from the mode functions $\tilde{f}_{\mathrm{LG}}$ and $\tilde{f}'_{\mathrm{LG}}$, together with the vectorial field structure of the focused vortex beam. The following analysis therefore concerns the local source pattern in the focal region; propagation and accumulated phase mismatch in an extended sample are not included.

The electric field vectors in (11) are given by

$$\mathbf{e}(\mathbf{r}) = \alpha\hat{\mathbf{x}} + \beta\hat{\mathbf{y}} + \hat{\mathbf{z}}\frac{i}{k}\left\{\alpha\left(\gamma\cos\phi - \frac{i\ell}{r}\sin\phi\right) + \beta\left(\gamma\sin\phi + \frac{i\ell}{r}\cos\phi\right)\right\}, \quad (12)$$

$$\bar{\mathbf{e}}'(\mathbf{r}) = \bar{\alpha}'\hat{\mathbf{x}} + \bar{\beta}'\hat{\mathbf{y}} - \hat{\mathbf{z}}\frac{i}{k'}\left\{\bar{\alpha}'\left(\bar{\gamma}'\cos\phi + \frac{i\ell'}{r}\sin\phi\right) + \bar{\beta}'\left(\bar{\gamma}'\sin\phi - \frac{i\ell'}{r}\cos\phi\right)\right\}, \quad (13)$$

where α and β specify the input transverse Jones state, while the full local polarization structure is contained in the complete vector field, including the longitudinal component. The two field contractions in Eq. (11) play distinct roles. The factor $\mathbf{e}\cdot\mathbf{e}$ determines whether the incident field can drive an isotropic electric-dipole THG source, and it is here that the longitudinal field component is essential. For a purely transverse circularly polarized plane wave, $\mathbf{e}_\perp\cdot\mathbf{e}_\perp = 0$, so the isotropic electric-dipole THG source vanishes. For the focused vortex field, however,

$$\mathbf{e}\cdot\mathbf{e} = \mathbf{e}_\perp\cdot\mathbf{e}_\perp + e_z^2,$$

so the longitudinal component supplies the nonzero term that leads to the circularly polarized result below. By contrast, $\mathbf{e}\cdot\bar{\mathbf{e}}'$ projects this nonlinear source onto the emitted harmonic polarization. In the far-field treatment used here, the emitted harmonic is taken to be transverse, so the final rate describes a longitudinally enabled nonlinear source coupled into a transverse radiated harmonic mode. For a linearly polarized input, the same longitudinal contribution modifies $\mathbf{e}\cdot\mathbf{e}$ through the azimuthally dependent terms in Eq. (16), producing the polarization-aligned lobes in Fig. 2.

A. Linear Polarization

We first consider THG with linearly polarized incident light. In this case, the polarization coefficients α and β are real, so the field carries no spin angular momentum. The spatial phase structure of the beam is determined solely by the orbital component $e^{i\ell\phi}$ associated with the vortex wavefront.

In the third-harmonic process, the nonlinear source term contains the product of three incident fields, giving an overall phase dependence proportional to $e^{i3(kz+\ell\phi)}$ (along with the wavefront curvature and the Gouy phase). Consequently, the emitted harmonic field must possess the longitudinal and azimuthal phase factors e^{i3kz} and $e^{i3\ell\phi}$ in order to satisfy phase matching and conservation of angular momentum. The emitted vortex mode therefore has azimuthal index $\ell' = 3\ell$.

We parameterize the linear polarization by an angle θ in the transverse plane such that

$$\alpha = \cos\theta, \quad (14)$$

$$\beta = \sin\theta, \quad (15)$$

where θ is measured with respect to the x axis. This provides a continuous description of linear polarization states from

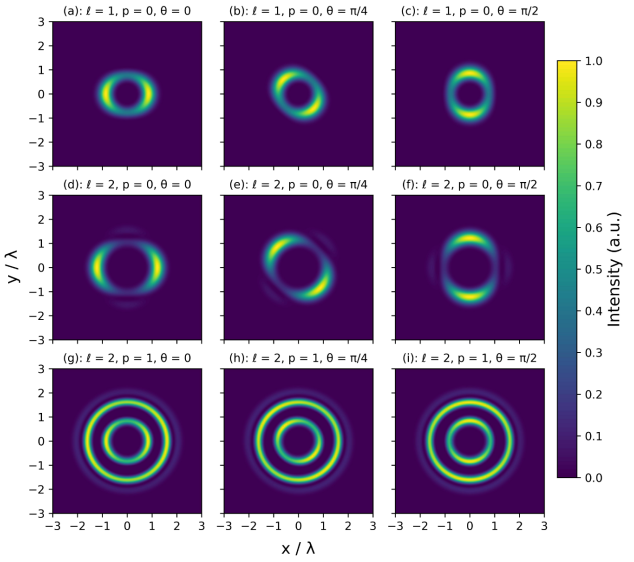

Fig. 2. Third-harmonic intensity distributions computed from Eq. (11) for varying ℓ, p, and θ. Each panel is normalized to its own maximum, with $\lambda = w_0$ throughout. Increasing ℓ broadens the ring structure, while increasing p introduces additional radial nodes. The intensity is asymmetric, with enhanced lobes aligned along the input polarization direction, and the overall pattern rotates with θ.

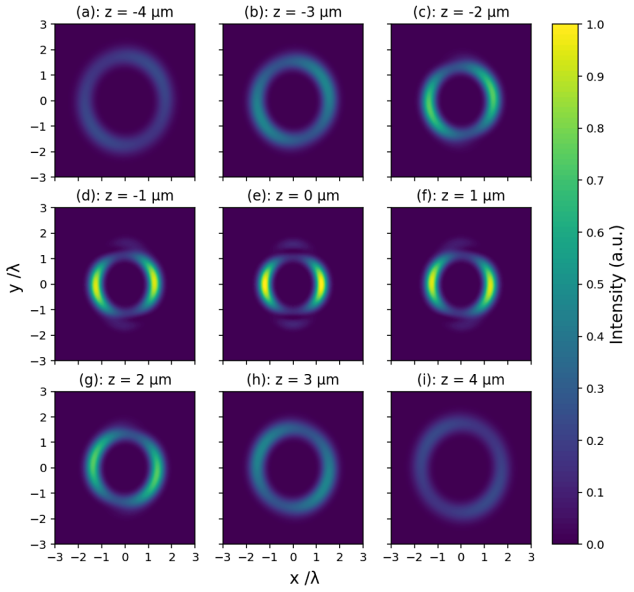

Fig. 3. Spatial intensity distributions along the direction of propagation for THG when $\ell = 2$ and $p = 0$, for an input beam with $\lambda = w_0$, and x-polarized incident and emission photons. The plots are normalized to the maximum of (e).

x polarization ($\theta = 0$) through diagonal to y polarization ($\theta = \pi/2$). In the expressions above, the incident field retains its longitudinal component, which arises from the nonparaxial structure of the focused beam and plays a key role in enabling the nonlinear interaction. For the emitted harmonic field, however, we restrict attention to the transverse radiation components. Although longitudinal field components may be present locally in the focal region, the propagating third-harmonic radiation detected in the far field is overwhelmingly transverse, with longitudinal contributions strongly suppressed as the beam approaches the paraxial regime. Accordingly, the longitudinal component of the emitted field is neglected in what follows, and the harmonic polarization is taken to lie in the transverse plane. We obtain

$$|\mathbf{e}\cdot\mathbf{e}|^2 = \left|1 + \frac{1}{k^2}\left[\frac{\ell^2}{r^2}\sin^2(\phi-\theta) - \gamma^2\cos^2(\phi-\theta) + i\gamma\frac{\ell}{r}\sin 2(\phi-\theta)\right]\right|^2, \tag{16}$$

with $|\mathbf{e}\cdot\bar{\mathbf{e}}'|^2 = 1$. Clearly, Eq. (16) contains no terms odd in ℓ, so the intensity distribution in Eq. (11) is invariant under $\ell \to -\ell$. The process therefore exhibits no chiral sensitivity, as expected on symmetry grounds. Substituting Eq. (16) into Eq. (11), the resulting intensity distributions for various values of θ are shown in Fig. 2. For $\ell \neq 0$, the emitted harmonic exhibits a vortex structure, while increasing p introduces radial nodes. The orientation of the input linear polarization gives rise to two clear features. First, the harmonic field is not circularly symmetric, exhibiting distinct lobes of high intensity aligned parallel to the input polarization direction. This behavior mirrors that observed in the linear intensity profile of tightly focused vortex beams [24] and originates from the nonparaxial longitudinal field components. Second, the spatial intensity distribution rotates with the polarization angle θ, again consistent with the behavior of the corresponding linear field.

Reversing the sign of ℓ produces identical intensity distributions for fixed p and z, confirming that the response depends only on $|\ell|$ and is independent of the handedness of the vortex, in agreement with Eq. (16). For larger values of ℓ and p [Figs. 2(d)–2(i)], the intensity patterns become increasingly structured. Bright rings sharpen and dominate, reflecting the scaling of the signal as $(\tilde{f}_{\mathrm{LG}})^6(\tilde{f}'_{\mathrm{LG}})^2$, which enhances peak regions. This behavior is consistent with the distinct roles of the LG mode indices. The radial index p controls the radial profile of the mode, including the number and position of radial nodes, whereas the vortex charge ℓ controls the azimuthal phase structure. The polarization-dependent asymmetry in Fig. 2 originates from the longitudinal field contribution and the polarization contractions in Eq. (16); it is therefore not expected to acquire a qualitatively new angular form simply by changing p. Within the present local source-intensity treatment, increasing p primarily redistributes the harmonic intensity radially, while propagation effects such as Gouy-phase mismatch may introduce additional p-dependent changes in an extended sample.

These results indicate that the spatial structure of the THG field can be systematically controlled through the mode indices ℓ and p, providing a route to tailoring harmonic beam profiles for applications in imaging and spectroscopy.

B. Evolution along *z*

Since these intensity distributions evolve along the propagation axis, the spatial dependence along the z axis may also be considered. Taking Fig. 2(d) as an example, Fig. 3 shows variations along the direction of propagation. It is emphasized that these results are obtained from the local nonlinear source intensity, and therefore implicitly assume effective phase matching of the generated harmonic field.

Figure 3(e) corresponds to Fig. 2(d). The remaining panels in Fig. 3 show the evolution of the local intensity distribution along the z axis. As z increases, the structure becomes less intricate and tends toward an approximately symmetric ring. This behavior is primarily governed by beam divergence and the changing balance between transverse and longitudinal field components. The apparent increase in radius reflects the natural spreading of the Laguerre–Gaussian mode.

Figures 3(e)–3(i) exhibit an apparent rotation of the intensity pattern, observable by tracking the points of maximum intensity. Pairing Figs. 3(a)–3(i), 3(b)–3(h), 3(c)–3(g), and 3(d)–3(f) shows that reversing the sign of z produces the same behavior with opposite handedness, consistent with the symmetry of the focused field.

It is also noted that more intricate structure is most evident for $z \lesssim z_R$. The Rayleigh range, $z_R = \frac{\pi w_0^2}{\lambda}$, sets the characteristic axial scale of the beam, and in the present case reduces to $z_R = \pi w_0 \approx 3.14\ \mu\text{m}$. Within this region, the field structure is dominated by the focal geometry.

Away from the focal plane, the Gouy phase introduces a mode-order-dependent axial phase mismatch between the nonlinear source and the generated harmonic field. As a result, coherent accumulation is reduced and the calculated intensity should be interpreted as a local source distribution rather than the fully propagated harmonic signal.

Accordingly, the discussion of Fig. 3 is most directly applicable to experiments probing the focal region or within the Rayleigh range. Beyond this regime, the observed behavior primarily reflects the evolution of the underlying beam structure, with reduced conversion efficiency expected due to incomplete phase matching.

C. Circular Polarization

We now consider the case of circularly polarized excitation. The polarization coefficients may be written as

$$\alpha = \frac{1}{\sqrt{2}}, \qquad \beta = \frac{i\sigma}{\sqrt{2}}, \tag{17}$$

where $\sigma = \pm 1$ denotes the helicity of the incident light. In contrast to the linear polarization case, the complex phase relation between the transverse field components corresponds to a nonzero spin angular momentum of $\sigma\hbar$ per photon.

For a purely transverse plane wave, the scalar product $(\mathbf{e}\cdot\mathbf{e})$ vanishes for circular polarization, preventing third-harmonic generation in an isotropic medium [4,36–38]. However, for a focused beam, the electric field possesses a longitudinal component arising from the nonparaxial structure of the mode. Substitution of the circular polarization coefficients into Eq. (12) shows that the surviving contribution to $(\mathbf{e}\cdot\mathbf{e})$ originates from this longitudinal field and carries an azimuthal phase dependence:

$$(\mathbf{e}\cdot\mathbf{e}) = -\frac{1}{2k^2}\left(\gamma - \frac{\sigma\ell}{r}\right)^2 e^{i2\sigma\phi}. \tag{18}$$

The nonlinear source term responsible for third-harmonic generation therefore carries the azimuthal phase factor $e^{i(3\ell+2\sigma)\phi}$. Phase matching then requires the emitted harmonic mode to possess corresponding longitudinal and azimuthal phase dependences with $k' = 3k$ and $\ell' = 3\ell + 2\sigma$, ensuring conservation of energy and total angular momentum of the radiation field. The vortex charge of the generated harmonic is therefore

$$\ell' = 3\ell + 2\sigma. \tag{19}$$

This condition also has a simple photon-level interpretation. Each incident circularly polarized vortex photon carries a total angular momentum projection $(\ell+\sigma)\hbar$ along the propagation axis. In the third-harmonic process, three such photons are annihilated, so the nonlinear source carries total angular momentum projection $3(\ell+\sigma)\hbar$. If the emitted third-harmonic photon has spin angular momentum $\sigma\hbar$, conservation of total angular momentum requires

$$3(\ell+\sigma) = \ell' + \sigma, \tag{20}$$

which gives $\ell' = 3\ell + 2\sigma$. Thus, the process should not be interpreted as separate conservation of spin and orbital angular momentum. Instead, the nonparaxial longitudinal field permits spin–orbit coupling, so that the two excess units of input spin angular momentum appear as orbital angular momentum of the emitted harmonic.

In the special case of a circularly polarized Gaussian input beam ($\ell = 0$), the generated third harmonic carries a vortex charge $\ell' = 2\sigma$. Thus, even without input OAM, a tightly focused circularly polarized beam can generate a vortex harmonic through spin–orbit interaction associated with the longitudinal field. This previously forbidden process therefore represents a further manifestation of spin–orbit interaction in light [39].

Again restricting attention to the transverse radiation components of the emitted harmonic field, we take $|\mathbf{e}\cdot\bar{\mathbf{e}}'|^2 = 1$, such that the remaining polarization dependence is fully contained in

$$|\mathbf{e}\cdot\mathbf{e}|^2 = \frac{1}{4k^4}\left|\gamma - \frac{\sigma\ell}{r}\right|^4. \tag{21}$$

This quantity may then be substituted into Eq. (11) to model third-harmonic generation driven by tightly focused circularly polarized Laguerre–Gaussian modes. The results are shown in Fig. 4. We emphasize that this electric-dipole contribution is not chiroptical. Although the field factor depends on $|\gamma - \sigma\ell/r|^4$ and therefore on the relative sign of spin and orbital angular momentum, this dependence arises from nonparaxial spin–orbit coupling rather than from molecular optical activity. It should therefore be distinguished from the E1–M1 contribution introduced in Section 3, which is odd under reversal of the relevant optical or material handedness and gives rise to genuine THVD.

First, for a Gaussian input beam, we find that circular polarization generates a vortex harmonic: an input LCP beam produces $\ell' = +2$, while an input RCP beam produces $\ell' = -2$, demonstrating that the sign of σ determines the sign of the generated topological charge. For vortex input beams ($\ell \neq 0$), we observe clear signatures of spin–orbit interaction [39]. In particular, the spatial structure of the harmonic depends on whether the spin and orbital angular momentum are parallel $(\text{sgn}\,\ell = \text{sgn}\,\sigma)$ or antiparallel $(\text{sgn}\,\ell \neq \text{sgn}\,\sigma)$, leading to

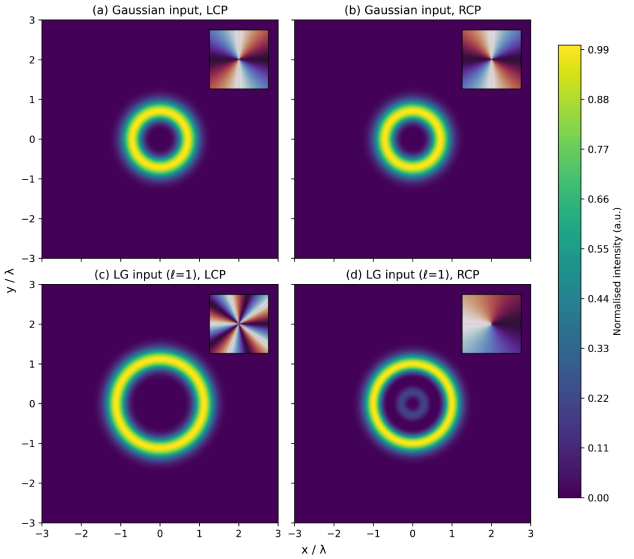

Fig. 4. Intensity of third-harmonic generation for the circularly polarized input (phase distributions shown in insets). (a), (b) For a Gaussian input ($\ell = 0$), the generated harmonic carries a vortex of charge $\ell' = \pm 2$, with the sign set by the input helicity σ, consistent with angular momentum conservation. (c), (d) For circularly polarized vortex beams, spin–orbit interaction emerges: parallel spin and OAM ($\sigma\ell > 0$) and antiparallel spin and OAM ($\sigma\ell < 0$) produce distinct radial intensity profiles. All panels are individually normalized, with $\lambda = w_0$.

distinct intensity distributions. This behavior is consistent with that observed in the linear regime for tightly focused vortex beams [24]. The additional radial rings and nodes that appear for some spin–orbit configurations are not associated with additional radial phase singularities. They arise from the radial weighting of the nonlinear source through the product of the LG mode factors and the nonparaxial spin–orbit factor $(\gamma - \sigma\ell/r)^4$. The phase inset therefore identifies the azimuthal phase structure of the generated harmonic, while the radial intensity profile is determined by the local source weighting.

We emphasize that, for plane-wave light and paraxial beams with purely transverse fields, third-harmonic generation with circularly polarized input is forbidden [3,36,37]. The non-zero response obtained here arises entirely from the longitudinal field component introduced by focusing. This contribution scales with the degree of nonparaxiality and vanishes in the paraxial limit.

3. THIRD-HARMONIC VORTEX DICHROISM

In the previous treatment of THG, all photon interactions with the molecules were assumed to be purely electric-dipole in nature. The circularly polarized THG channel identified in Section 2 is therefore an allowed electric-dipole process enabled by the longitudinal field component of the focused beam; it is not, by itself, a chiroptical effect, since the electric-dipole response contains no molecular pseudoscalar and is insensitive to molecular handedness. Although the electric-dipole contributions in Eq. (1) are typically orders of magnitude larger than the corresponding magnetic-dipole terms, the latter enable chiral molecules to exhibit optical activity [4,26]. In this section, we show that interference between electric- and magnetic-dipole contributions introduces a chiral component into the nonlinear scattering amplitude, giving rise to third-harmonic vortex dichroism (THVD) in isotropic chiral media. Here, THVD denotes the component of the third-harmonic response that is odd under reversal of the vortex handedness, $\ell \to -\ell$, for fixed input polarization and fixed molecular enantiomer. This distinguishes a genuine vortex-handedness response from spin–orbit-dependent reshaping of the third-harmonic field, which may depend on the relative sign of $\sigma\ell$ but is not, by itself, a vortex dichroism.

One important manifestation of linear optical activity is circular dichroism: the differential absorption of right- and left-handed circularly polarized light by chiral molecules. This phenomenon forms the basis of chiroptical spectroscopy, an incisive all-optical method for determining the absolute handedness of pharmaceuticals and other biologically relevant molecules [25,40,41]. As discussed in the previous section, under typical illumination conditions third-harmonic generation is forbidden for circularly polarized light in isotropic media [36–38], and consequently no analogous THG chiroptical effect has previously been identified. In this section, we show that optical activity can in fact arise in third-harmonic generation when vortex light is employed. For linearly polarized vortex beams, this gives rise to third-harmonic vortex dichroism (THVD), while circularly polarized excitation leads to a related spin–orbit-modified chiroptical THG response.

The first step in deriving the scattered intensity for THVD involves modifying the time-ordered Feynman diagrams used for THG. Specifically, by replacing one electric-dipole coupling with a magnetic-dipole coupling, and repeating this process for all permutations of the photon interactions (see Supplement 1), the matrix element is obtained as

$$
\begin{aligned}
M_{FI} = -\left(\frac{\hbar c}{2\epsilon_0 V}\right)^2 (k^3 k')^{\frac{1}{2}} \sqrt{n(n-1)(n-2)} \\
\times \sum_{\xi} \overline{\tilde{f}'_{\mathrm{LG}}(r_\xi, z_\xi)}\, \tilde{f}^{3}_{\mathrm{LG}}(r_\xi, z_\xi)\, \mathrm{e}^{i\Delta\Phi(r_\xi,\phi_\xi,z_\xi)} \Big[c\bar{e}'_i e_j e_k e_l \beta_{ijkl}(\xi) \\
+ \bar{b}'_i e_j e_k e_l G_{ijkl}(\xi) + \bar{e}'_i b_j e_k e_l H_{ijkl}(\xi) + \bar{e}'_i e_j b_k e_l I_{ijkl}(\xi) \\
+ \bar{e}'_i e_j e_k b_l J_{ijkl}(\xi) \Big],
\end{aligned}
\tag{22}
$$

where $\Delta\Phi(r_\xi, \phi_\xi, z_\xi)$ is the phase mismatch defined in (6), evaluated at molecular center ξ. b_i represents the magnetic field vector of photon i. G_{ijkl}, H_{ijkl}, I_{ijkl}, and J_{ijkl} are purely imaginary fourth-rank tensors corresponding to the light–matter interaction pathways illustrated in Supplement 1. The full expressions for these tensors are provided in Supplement 1. Using (22), and exploiting similarities between the H_{ijkl}, I_{ijkl}, and J_{ijkl} tensors, the rotationally averaged intensity distribution is given by

$$I_{\mathrm{THG}}^{\mathrm{E1}^4+\mathrm{E1}^3\mathrm{M1}} = \frac{9\bar{I}_0^3 g^{(3)} k^4 N_{\mathrm{eff}}^2}{6400\pi^2\varepsilon_0^4 c^4} \tilde{f}_{\mathrm{LG}}^6 \tilde{f}_{\mathrm{LG}}'^2 \Big| 6c(\mathbf{e}\cdot\mathbf{e})(\mathbf{e}\cdot\bar{\mathbf{e}}')\beta_{\lambda\lambda\mu\mu} + 6(\mathbf{e}\cdot\mathbf{e})(\mathbf{e}\cdot\bar{\mathbf{b}}')G_{\lambda\lambda\mu\mu} + (\mathbf{e}\cdot\mathbf{e})(\mathbf{b}\cdot\bar{\mathbf{e}}')\Big(H_{\lambda\lambda\mu\mu} + 3H_{\mu\lambda\lambda\mu} + 2H_{\lambda\mu\mu\lambda}\Big) + (\mathbf{b}\cdot\mathbf{e})(\mathbf{e}\cdot\bar{\mathbf{e}}')\Big(7H_{\lambda\lambda\mu\mu} + H_{\mu\lambda\lambda\mu} + 4H_{\lambda\mu\mu\lambda}\Big)\Big|^2. \tag{23}$$

The notation $I_{\mathrm{THG}}^{\mathrm{E1}^4+\mathrm{E1}^3\mathrm{M1}}$ indicates that the scattering amplitude has been retained through the pure electric-dipole contribution and the terms containing one magnetic-dipole interaction. Further details of the rotational average can be found in Supplement 1. The first term in the vertical bars in (23) is simply the electric-dipole contribution to the THG scattering intensity from the previous section. It is established that the origin of natural optical activity arises from the interference between electric-dipole couplings (E1) with both magnetic-dipole (M1) and electric-quadrupole (E2) couplings [42]. The orientational average of the fifth-rank tensor associated with the E1–E2 interaction vanishes for an isotropic molecular ensemble. This follows because no isotropic tensor of odd rank can be formed from Kronecker delta invariants, and hence the rotational average of the E1–E2 contribution is identically zero. This justifies why we have concentrated solely on dipole coupling.

Therefore only E1–M1 contributions will be considered, justifying the earlier truncation of the multipolar interaction Hamiltonian to dipolar coupling. To identify the terms responsible for third-harmonic optical activity, the relevant cross terms with an overall odd parity must be isolated. Electric-dipole interactions have odd parity, whereas magnetic-dipole interactions have even parity. Consequently, the tensor $\beta_{\lambda\lambda\mu\mu}$, containing four electric-dipole interactions, possesses overall even parity, while the remaining tensors acquire odd parity through the introduction of a single magnetic-dipole interaction. The chiroptical response therefore arises from terms containing one **b** vector, since an overall odd parity to leading order requires an odd number of electric-field factors combined with a single magnetic-field contribution. In the leading-order chiral contribution, six distinct contributing terms remain, which can be grouped into three pairs:

$$I_{\mathrm{THG}}^{\mathrm{E1}^4-\mathrm{E1}^3\mathrm{M1}} = \frac{27\bar{I}_0^3 g^{(3)} k^4 N_{\mathrm{eff}}^2}{1600\pi^2\varepsilon_0^4 c^3} \beta_{\lambda\lambda\mu\mu} \tilde{f}_{\mathrm{LG}}^6 \tilde{f}_{\mathrm{LG}}'^2 \times \mathrm{Re}\Big[6|\mathbf{e}\cdot\mathbf{e}|^2(\bar{\mathbf{e}}\cdot\mathbf{e}')(\mathbf{e}\cdot\bar{\mathbf{b}}')G_{\lambda\lambda\mu\mu} + |\mathbf{e}\cdot\mathbf{e}|^2(\bar{\mathbf{e}}\cdot\mathbf{e}')(\mathbf{b}\cdot\bar{\mathbf{e}}')\Big(H_{\lambda\lambda\mu\mu} + 3H_{\mu\lambda\lambda\mu} + 2H_{\lambda\mu\mu\lambda}\Big) + |\mathbf{e}\cdot\bar{\mathbf{e}}'|^2(\bar{\mathbf{e}}\cdot\bar{\mathbf{e}})(\mathbf{b}\cdot\mathbf{e})\Big(7H_{\lambda\lambda\mu\mu} + H_{\mu\lambda\lambda\mu} + 4H_{\lambda\mu\mu\lambda}\Big)\Big]. \tag{24}$$

Equation (24) is therefore the leading chiral E1–M1 interference contribution extracted from Eq. (23). In the linearly polarized case considered below, this term gives the THVD contribution. To leading order in the magnetic-dipole coupling, the third-harmonic generation intensity may be written schematically as

$$I_{\mathrm{THG}} \simeq I_{\mathrm{THG}}^{\mathrm{achiral}} + I_{\mathrm{THG}}^{\mathrm{E1}^4-\mathrm{E1}^3\mathrm{M1}}, \tag{25}$$

where $I_{\mathrm{THG}}^{\mathrm{achiral}}$ denotes the electric-dipole-dominated achiral third-harmonic intensity and $I_{\mathrm{THG}}^{\mathrm{E1}^4-\mathrm{E1}^3\mathrm{M1}}$ denotes the leading chiral E1–M1 interference contribution. Terms containing two or more magnetic-dipole interactions are higher order in the multipolar expansion and are neglected.

In the previous treatment of THG, all contributing terms depended solely on the electric-field polarization vectors **e**. Since electric-dipole interactions possess odd parity, combinations involving only electric fields yield an overall even parity and therefore cannot give rise to chiral effects. In (24), however, terms appear that contain magnetic-field vectors **b**, enabling optical activity through electric–magnetic dipole interference.

A. Linear Polarization

We now focus on linearly polarized input beams. In this case, the circular-polarization helicity σ vanishes, removing any chirality associated with the spin angular momentum of the field. Consequently, any non-zero chiroptical signal must originate solely from the handedness of the optical wavefront, characterized by the pseudoscalar vortex charge ℓ.

We once again parameterize the incident linearly polarized field by an angle θ in the transverse plane as $\mathbf{e} = \cos\theta\,\hat{\mathbf{x}} + \sin\theta\,\hat{\mathbf{y}}$, with the corresponding magnetic field orthogonal to **e** and also confined to the transverse plane. As in the preceding THG analysis, we restrict attention to the transverse radiation components of the emitted harmonic field, neglecting the longitudinal component that arises locally from the nonlinear source but is strongly suppressed in the far-field propagation. The detected harmonic is taken to share the same transverse polarization as the incident field, so that $\bar{\mathbf{e}}' \parallel \mathbf{e}$ and $\bar{\mathbf{b}}'$ remain orthogonal to $\bar{\mathbf{e}}'$. Under these conditions, the mixed contractions $\mathbf{e}\cdot\bar{\mathbf{b}}'$ and $\mathbf{b}\cdot\bar{\mathbf{e}}'$ vanish by orthogonality, leaving the only surviving electric–magnetic contribution proportional to $(\mathbf{b}\cdot\mathbf{e})(\bar{\mathbf{e}}\cdot\bar{\mathbf{e}})$.

The magnetic-field vectors appearing in (24) are given by

$$\mathbf{b}(\mathbf{r}) = \alpha\hat{\mathbf{y}} - \beta\hat{\mathbf{x}} + \hat{\mathbf{z}}\frac{i}{k}\left\{\alpha\left(\gamma\sin\phi + \frac{i\ell}{r}\cos\phi\right) - \beta\left(\gamma\cos\phi - \frac{i\ell}{r}\sin\phi\right)\right\}, \tag{26}$$

$$\bar{\mathbf{b}}'(\mathbf{r}) = \bar{\alpha}'\hat{\mathbf{y}} - \bar{\beta}'\hat{\mathbf{x}}. \tag{27}$$

Using these vectors yields

$$(\mathbf{b}\cdot\mathbf{e}) = \frac{1}{k^2}\left[\left(\gamma^2+\frac{\ell^2}{r^2}\right)\left(\alpha\beta\cos 2\phi - \frac{1}{2}(\alpha^2-\beta^2)\sin 2\phi\right) + i\frac{\gamma\ell}{r}\left((\beta^2-\alpha^2)\cos 2\phi - 2\alpha\beta\sin 2\phi\right)\right]. \tag{28}$$

It is noteworthy that the transverse electric and magnetic field components are identically orthogonal for arbitrary Jones coefficients α and β, as required by Maxwell's equations for a propagating beam. Consequently, $(\mathbf{b}\cdot\mathbf{e})$ receives contributions only from the longitudinal field components associated with the nonparaxial structure of the beam.

The next step is to combine all polarization inner products appearing in the non-zero term of Eq. (24). Assuming again that the emitted harmonic is probed in the far field, we have trivially $|\mathbf{e}\cdot\bar{\mathbf{e}}'|^2 = 1$, leaving the product $(\bar{\mathbf{e}}\cdot\bar{\mathbf{e}})(\mathbf{b}\cdot\mathbf{e})$. For a general linear polarization state, parameterized by the angle θ, this quantity can be written compactly in terms of the relative azimuthal coordinate $\phi-\theta$. At the focal plane, $z=0$, where γ is real, we obtain

$$\begin{aligned}&(\mathbf{b}\cdot\mathbf{e})(\bar{\mathbf{e}}\cdot\bar{\mathbf{e}})\\ &= -\frac{1}{k^2}\left[\frac{1}{2}\left(\gamma^2+\frac{\ell^2}{r^2}\right)\sin 2(\phi-\theta) + i\gamma\frac{\ell}{r}\cos 2(\phi-\theta)\right]\\ &\quad\times\left[1+\frac{1}{k^2}\left(\frac{\ell^2}{r^2}\sin^2(\phi-\theta) - \gamma^2\cos^2(\phi-\theta) - i\gamma\frac{\ell}{r}\sin 2(\phi-\theta)\right)\right].\end{aligned} \tag{29}$$

Here, θ denotes the angle of the input linear polarization with respect to the x axis, such that $\theta=0$ corresponds to x polarization, $\theta=\pi/4$ to diagonal polarization, and $\theta=\pi/2$ to y polarization.

The observable intensity is determined by the real part of the field-molecular product. The tensor combination

$$7H_{\lambda\lambda\mu\mu} + H_{\lambda\mu\lambda\mu} + 4H_{\lambda\mu\mu\lambda} = i\,\mathcal{H}, \qquad \mathcal{H}\in\mathbb{R}$$

is purely imaginary, as expected for magnetic-dipole contributions. The relevant term is therefore proportional to the negative imaginary part of the field factor, since $\mathrm{Re}[i\mathcal{H}F] = -\mathcal{H}\,\mathrm{Im}(F)$, where $F = (\bar{\mathbf{e}}\cdot\bar{\mathbf{e}})(\mathbf{b}\cdot\mathbf{e})$:

$$\Im\left[(\bar{\mathbf{e}}\cdot\bar{\mathbf{e}})(\mathbf{b}\cdot\mathbf{e})\right] = -\frac{\gamma\ell}{k^2 r}\cos 2(\phi-\theta) + \frac{\gamma\ell}{k^4 r}\left[\gamma^2\cos^2(\phi-\theta) + \frac{\ell^2}{r^2}\sin^2(\phi-\theta)\right]. \tag{30}$$

The linear dependence on ℓ shows that the signal reverses with the handedness of the optical vortex. The resulting THVD intensity is

$$\begin{aligned}I_{\mathrm{THVD}}^{\mathrm{lin}} &= \frac{27\bar{I}_0^3 g^{(3)} k^4 N_{\mathrm{eff}}^2}{1600\pi^2\varepsilon_0^4 c^3}\,\beta_{\lambda\lambda\mu\mu}\,\tilde{f}_{\mathrm{LG}}^6\tilde{f}_{\mathrm{LG}}^{\prime 2}\,\mathcal{H}\\ &\quad\times\left[\frac{\gamma\ell}{k^2 r}\cos 2(\phi-\theta) - \frac{\gamma\ell}{k^4 r}\right.\\ &\quad\left.\times\left(\gamma^2\cos^2(\phi-\theta) + \frac{\ell^2}{r^2}\sin^2(\phi-\theta)\right)\right].\end{aligned} \tag{31}$$

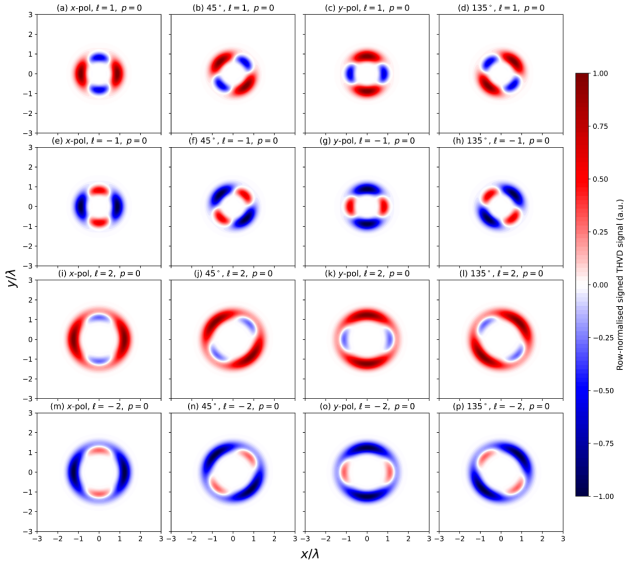

Fig. 5. Spatial distribution of the THVD signal computed from Eq. (31) for varying ℓ and θ. The sign of the distribution reverses with the handedness of ℓ and rotates with θ. In all cases, the spatially integrated signal is non-zero, with the effect becoming more pronounced for larger ℓ. All panels are individually normalized, with $\lambda = w_0$.

Using (31) as the framework to model THVD in fluids, Fig. 5 shows the spatial distribution in the focal plane of this process. For clarity, all molecular response tensors are taken to be equal in magnitude in the simulations presented here for illustrative purposes, and this assumption is maintained throughout the paper. A fully quantitative treatment for a specific system would require evaluation of these tensors using quantum chemical methods, which is beyond the scope of this work. Since all contributing tensor terms enter with the same polarization structure under the conditions considered here (far-field detection of the transverse harmonic field), their relative magnitudes do not alter the qualitative form of the spatial distributions, but only rescale the overall signal. The results therefore capture the general, field-driven features of the response, governed by symmetry and the structure of the light–matter interaction rather than by molecule-specific tensor values.

The spatial distributions shown in Fig. 5 represent the signed THVD signal for varying input polarization angle θ and topological charge ℓ, with $p=0$. A prominent feature is the appearance of alternating positive and negative lobes arranged azimuthally about the beam axis. A defining property of these distributions is their odd dependence on ℓ. Comparison of rows corresponding to ℓ and $-\ell$ shows identical spatial structure with complete sign reversal, such that regions of positive and negative signal are interchanged. This confirms that the THVD signal is linear in ℓ, and therefore directly encodes the handedness of the optical vortex. In contrast to the achiral THG intensity, which depends only on $|\ell|$, the THVD response is intrinsically sensitive to the sign of the topological charge.

The orientation of the lobes is set by the input polarization angle θ. Varying θ rotates the entire THVD pattern, consistent with the angular dependence in Eq. (31). A similar angle-dependent response has been reported in two-photon absorption of vortex beams [29], in contrast to the circular

symmetry typical of the linear regime. Increasing $|\ell|$ modifies the spatial structure while preserving its symmetry. For $|\ell| = 1$, the signal consists of broader lobes, whereas for $|\ell| = 2$, the distribution becomes more sharply defined and ring-like, with enhanced contrast at larger radii. This reflects the underlying Laguerre–Gaussian mode structure, with the THVD signal inheriting both the radial redistribution of intensity and the azimuthal phase structure.

The resulting patterns are symmetric in magnitude but antisymmetric in sign, consistent with the pseudoscalar character of the E1M1 term. Nodal lines separating regions of opposite sign correspond to directions along which the chiral contribution vanishes. Overall, these results demonstrate that THVD provides a spatially resolved chiral observable in isotropic media, in which the vortex handedness determines the sign of the response while the input polarization controls its orientation.

Unlike linear chiroptical measures, nonlinear optical signals do not admit a conserved electromagnetic pseudoscalar analogous to optical chirality [43,44]. Optical chirality arises from the duality symmetry of Maxwell's equations and is quadratic in the fields, such that for linearly polarized beams its spatial integral vanishes even in the presence of longitudinal field components [23,24].

In contrast, the present third-harmonic vortex dichroism signal originates from higher-order field-matter interactions, involving products of three electric fields and one magnetic field. The resulting pseudoscalar is therefore not a property of the electromagnetic field alone, but of the combined light–matter interaction. As a consequence, there is no symmetry constraint enforcing cancellation of the spatial integral. The nonlinear interaction effectively converts the structured, but globally achiral, field into a non-vanishing pseudoscalar observable. Accordingly, the integrated signal can remain finite even for the linearly polarized input, with its sign determined by the vortex charge ℓ.

B. Circular Polarization: Spin–Orbit-Modified Chiroptical THG

Having established that a non-zero THVD signal can arise even in the absence of helicity σ associated with polarization, we now consider circularly polarized excitation. In contrast to the linearly polarized case examined above, circular polarization introduces an intrinsic electromagnetic handedness associated with the spin angular momentum of the field. The resulting chiroptical response therefore reflects a nonparaxial coupling between the spin helicity σ and the orbital angular momentum of the vortex beam characterized by the topological charge ℓ. In this regime, the chiroptical THG signal is no longer determined solely by the wavefront structure of the optical vortex, but instead arises from the coupling of the circular polarization state to the azimuthal phase structure via the longitudinal field components. This spin–orbit interaction is encoded through the combination $(\gamma - \sigma\ell/r)$, which modifies the spatial weighting of the signal. Substituting the circular polarization coefficients $\alpha = 1/\sqrt{2}$ and $\beta = i\sigma/\sqrt{2}$ into the general leading E1–M1 interference contribution in Eq. (24), and again retaining the transverse emitted harmonic component, gives

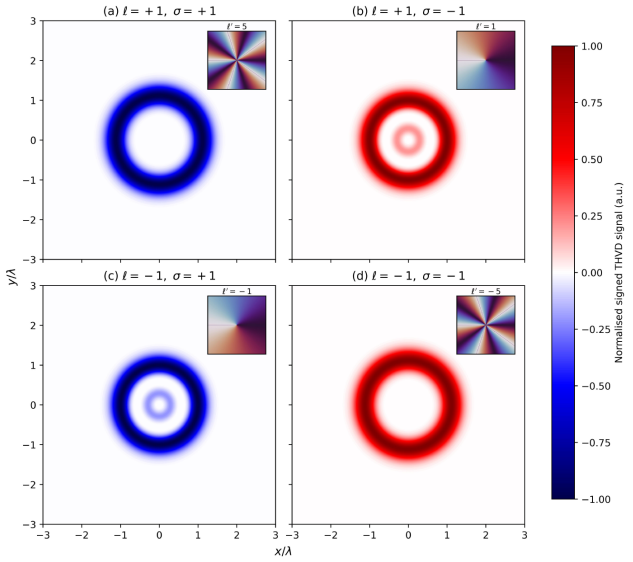

Fig. 6. Intensity of the circularly polarized chiroptical THG signal computed from Eq. (32). The response arises from E1–M1 interference and contains an explicit helicity dependence, while the vortex charge modifies the radial profile through the nonparaxial spin–orbit factor $(\gamma - \sigma\ell/r)^4$. Unlike the linearly polarized THVD signal, the circularly polarized response is not purely odd in ℓ. All panels are individually normalized, with $\lambda = w_0$.

$$I^{\mathrm{circ}}_{\mathrm{THG,chiral}} = \frac{27\bar{I}_0^3 g^{(3)} N_{\mathrm{eff}}^2}{6400\pi^2\varepsilon_0^4 c^3}\,\beta_{\lambda\lambda\mu\mu}\,\tilde{f}^6_{\mathrm{LG}}\tilde{f}^{*2}_{\mathrm{LG}}\,\delta_{\sigma\sigma'} \times \mathrm{Re}\left[i\sigma\left(\gamma - \frac{\sigma\ell}{r}\right)^4 \left(6G_{\lambda\lambda\mu\mu} - 8H_{\lambda\lambda\mu\mu} - 4H_{\lambda\mu\lambda\mu} - 6H_{\lambda\mu\mu\lambda}\right)\right]. \quad (32)$$

The spatial distributions corresponding to Eq. (32) are shown in Fig. 6. In contrast to the linearly polarized THVD case, the circularly polarized chiroptical THG signal exhibits a clear spin–orbit interaction between σ and ℓ. The global sign of the response is determined primarily by the helicity σ, while the vortex charge ℓ modifies the spatial structure through the radial factor $(\gamma - \sigma\ell/r)^4$. As a result, changing the sign of ℓ does not simply invert the signal, but instead reshapes the radial profile through the spin–orbit interaction.

A further striking feature is the emergence of radially symmetric, ring-like intensity profiles. Unlike the azimuthally structured patterns observed for linear polarization, the circularly polarized case produces distributions that are independent of the azimuthal angle ϕ. This reflects the absence of a preferred transverse direction in circular polarization, with the spin angular momentum imposing rotational symmetry on the response. The circularly polarized chiroptical THG signal is therefore primarily encoded in the radial dependence of the field, rather than in angular modulation.

The influence of spin–orbit interaction is evident when comparing different combinations of σ and ℓ. For a given helicity σ, varying the sign and magnitude of ℓ redistributes the intensity radially: some configurations produce a single dominant ring, whereas others generate an additional inner structure. This

behavior is consistent with the form of Eq. (32), in which the factor $(\gamma - \sigma\ell/r)^4$ modifies the radial weighting of the signal through the nonparaxial interaction of spin helicity and orbital angular momentum. The additional radial rings and nodes therefore arise from the local source weighting, rather than from additional radial phase singularities. Reversing both the spin helicity σ and the vortex charge ℓ produces a complete inversion of the circularly polarized chiroptical THG signal while preserving the spatial structure. This spin–orbit behavior mirrors that of CPL-driven THG in Fig. 4.

Overall, these results show that circularly polarized excitation leads to a related but distinct chiroptical THG regime. The response arises from E1–M1 interference and contains an explicit helicity factor σ, while its radial structure is modified by the nonparaxial spin–orbit factor $(\gamma - \sigma\ell/r)^4$. Thus, unlike the linearly polarized THVD signal, the circularly polarized response is not purely odd in ℓ. Instead, its sign is controlled by the input helicity and the molecular enantiomer, while the vortex charge enters through spin–orbit-dependent reshaping of the radial profile.

4. DISCUSSION AND CONCLUSION

Third-harmonic generation in isotropic molecular fluids is a non-chiroptical process, dominated by the electric-dipole $\chi^{(3)}$ response and insensitive to molecular handedness [3,4]. Moreover, for circularly polarized plane waves, the process is angular-momentum forbidden, so that no conventional third-harmonic analog of circular dichroism has been available in such media [36,37]. The present work shows that both of these limitations can be overcome by structured light. In particular, the nonparaxial longitudinal field components of focused Laguerre–Gaussian beams permit third-harmonic generation with circularly polarized excitation in an isotropic fluid, establishing a mechanism that is unavailable for plane-wave or purely transverse fields. This significantly broadens the known symmetry landscape of THG in molecular media. A closely related effect was recently demonstrated in an optical nanofiber, where confinement-induced photonic spin–orbit interaction allows a circularly polarized Gaussian pump to drive third-harmonic generation into an optical vortex mode that would be forbidden in an isotropic bulk medium under conventional conditions [45]. In that case, the key physics is that subwavelength confinement generates spin–orbit-entangled eigenmodes, so that total angular momentum remains the relevant conserved quantity even though spin and orbital angular momenta are no longer separately conserved. The present results point to the same underlying origin, namely spin–orbit interaction, but in our case, this arises through the structured and tightly focused optical field itself rather than through nanofiber-guided mode confinement. Indeed, third-harmonic generation from circularly polarized light has previously been observed under tight focusing, where the effect was attributed to depolarization of the field [46]. While this was not framed in terms of optical angular momentum, the present results suggest that such observations can be understood more generally as manifestations of spin–orbit interaction. Taken together, these studies show that the apparent lifting of conventional CPL-based selection rules in THG is a genuine signature of spin–orbit coupling, and not something unique to one specific platform. Related angular-momentum selection rules have recently been explored in nonlinear flat optics, where Menshikov *et al.* demonstrated third-harmonic light structuring through total-angular-momentum projection addition in an amorphous-silicon thin film [47]. That system is distinct from the isotropic molecular media considered here, since the measured response is governed by a thin-film geometry with interfaces, boundary conditions, and propagation of the generated harmonic field. Nevertheless, it reinforces the broader point that, for focused structured fields, total angular momentum rather than separately conserved spin and orbital angular momenta provides the natural organizing principle for nonlinear harmonic generation.

The scope of the present theory should also be distinguished from nonlinear optical processes in nanostructured or strongly inhomogeneous environments. Here, the radiation field is treated as a prescribed focused Laguerre–Gaussian mode in a homogeneous background, and the material response enters through molecular response tensors contracted with the local optical field. The general scattering amplitude before orientational averaging is not restricted to isotropic fluids: for oriented molecular media, molecular crystals, films, or partially ordered solids, the full laboratory-frame tensor contractions may be retained, or averaged over the relevant orientational distribution. The isotropic rotational averages used in Eqs. (11) and (23) correspond specifically to randomly oriented molecular ensembles, such as dilute gases, isotropic molecular liquids, dilute chiral solutions, and amorphous molecular media where no preferred molecular orientation is present.

By contrast, in nanoparticles, metasurfaces, cavities, interfaces, or strongly dispersive media, the photonic environment can substantially modify both the local driving field and the emitted harmonic radiation. In such cases, the appropriate formulation would replace the free-space mode expansion by a dyadic Green's function or a normal-mode treatment of the electromagnetic environment, together with the relevant material symmetry or orientational distribution. The present results therefore establish free-space molecular selection rules and field-structure dependence in the isotropic limit, while providing a starting point for extensions to oriented condensed-phase and nanostructured systems.

Beyond this, we have shown that optical vortices enable the first chiroptical analog of third-harmonic generation in isotropic molecular fluids. Through electric-dipole–magnetic-dipole interference, the generated third-harmonic signal acquires a contribution that is odd in the vortex charge and reverses sign upon inversion of either ℓ or molecular handedness. This third-harmonic vortex dichroism therefore constitutes, to our knowledge, the first viable mechanism for chiral discrimination in THG from an isotropic fluid. In contrast to conventional chiroptical effects based on circular polarization, this regime can be driven by the handedness of the wavefront itself, with orbital angular momentum providing a key control parameter. We also identify a complementary regime in which a circularly polarized input gives a spin–orbit-modified chiroptical THG signal, whose sign is governed by the helicity σ and molecular handedness, while the vortex charge reshapes the radial profile.

A notable consequence is that chiral-sensitive third-harmonic signals can be generated in randomly oriented media using

both linearly polarized and circularly polarized vortex beams. The former represents a qualitatively distinct operating regime from standard circular-dichroism-based methods, emerging from the combined presence of longitudinal field components, transverse inhomogeneity, and geometric chirality in structured light. The sign and spatial form of the THVD signal can in principle be tuned through the vortex indices, suggesting a route to mode-resolved nonlinear chiroptical spectroscopy. Chiroptical nonlinear techniques are an active area of research, particularly in second- and third-order harmonic scattering in molecules and nanostructures [48–53]. Previous reports of optical activity in third-harmonic Rayleigh scattering from isotropic suspensions of chiral nanostructures interpreted the observed contrast within a framework where circularly polarized THG is strongly constrained by angular-momentum selection rules [51]. That process is distinct from the coherent THG source considered here, but the present result shows that this selection-rule argument is not generally valid once the driving field has an appreciable longitudinal and spin–orbit structure.

The spatial structure of the predicted signals also points to possible applications beyond bulk spectroscopy. Since THG is intrinsically sensitive to the local field structure and is often the strongest near boundaries and regions of optical inhomogeneity, vortex-driven THG and THVD may furnish new forms of spatially resolved nonlinear imaging in molecular fluids, soft matter, and interfacial environments. In such settings, the combination of harmonic contrast with sensitivity to vortex handedness could provide information not accessible to standard THG, while the circularly polarized THG channel identified here offers an additional means of controlling the generated harmonic mode through spin–orbit interaction.

Overall, these results show that structured light does more than modify the spatial profile of third-harmonic generation: it changes which nonlinear optical processes are allowed in isotropic molecular media. Focused optical vortices permit both the generation of third harmonics with circularly polarized excitation, previously deemed forbidden, and the emergence of a genuinely chiroptical third-harmonic response. Together, these findings expand the foundations of nonlinear molecular optics and identify orbital angular momentum and spin–orbit interaction as powerful degrees of freedom for controlling and probing harmonic generation in fluid media.

Disclosures. The authors declare no conflicts of interest.

Data availability. Data underlying the results presented in this paper are not publicly available at this time but may be obtained from the authors upon reasonable request.

Supplemental document. See Supplement 1 for supporting content.

REFERENCES

1. B. Gu, C. Zhao, A. Baev, *et al.*, "Molecular nonlinear optics: recent advances and applications," Adv. Opt. Photonics **8**, 328–369 (2016).
2. J. Zyss, *Molecular Nonlinear Optics: Materials, Physics, and Devices* (Academic Press, 2013).
3. D. L. Andrews and P. Allcock, *Optical Harmonics in Molecular Systems: Quantum Electrodynamical Theory* (Wiley Online Library, 2002), Vol. **1**.
4. D. P. Craig and T. Thirunamachandran, *Molecular Quantum Electrodynamics: an Introduction to Radiation-Molecule Interactions* (Courier Corporation, 1998).
5. W. R. Zipfel, R. M. Williams, and W. W. Webb, "Nonlinear magic: multiphoton microscopy in the biosciences," Nat. Biotechnol. **21**, 1369–1377 (2003).
6. C.-H. Yu, S.-P. Tai, C.-T. Kung, *et al.*, "Molecular third-harmonic-generation microscopy through resonance enhancement with absorbing dye," Opt. Lett. **33**, 387–389 (2008).
7. D. Smirnova, S. Kruk, D. Leykam, *et al.*, "Third-harmonic generation in photonic topological metasurfaces," Phys. Rev. Lett. **123**, 103901 (2019).
8. L. Bonacina, P.-F. Brevet, M. Finazzi, *et al.*, "Harmonic generation at the nanoscale," J. Appl. Phys. **127**, 230901 (2020).
9. C. Xu, M. Nedergaard, D. J. Fowell, *et al.*, "Multiphoton fluorescence microscopy for in vivo imaging," Cell **187**, 4458–4487 (2024).
10. E. O. Potma, *Foundations of Nonlinear Optical Microscopy* (John Wiley & Sons, 2024).
11. O. Faucher, E. Prost, E. Hertz, *et al.*, "Rotational Doppler effect in harmonic generation from spinning molecules," Phys. Rev. A **94**, 051402 (2016).
12. D. S. Bradshaw, K. A. Forbes, and D. L. Andrews, "Off-resonance control and all-optical switching: expanded dimensions in nonlinear optics," Appl. Sci. **9**, 4252 (2019).
13. W. T. Buono and A. Forbes, "Nonlinear optics with structured light," Opto-Electron. Adv. **5**, 210174 (2022).
14. Y.-C. Lou, Z.-M. Cheng, Z.-H. Liu, *et al.*, "Third-harmonic generation of spatially structured light in a quasi-periodically poled crystal," Optica **9**, 183–186 (2022).
15. S. Singh and A. Forbes, "Progress in structured light with nonlinear optics," Prog. Electromagn. Res. **185**, 1–16 (2026).
16. A. Forbes, M. de Oliveira, and M. R. Dennis, "Structured light," Nat. Photonics **15**, 253–262 (2021).
17. C. He, Y. Shen, and A. Forbes, "Towards higher-dimensional structured light," Light. Sci. Appl. **11**, 205 (2022).
18. D. L. Andrews and M. Babiker, *The Angular Momentum of Light* (Cambridge University Press, 2012).
19. Y. Shen, X. Wang, Z. Xie, *et al.*, "Optical vortices 30 years on: OAM manipulation from topological charge to multiple singularities," Light. Sci. Appl. **8**, 90 (2019).
20. A. Salam, *Molecular Quantum Electrodynamics: Long-Range Intermolecular Interactions* (John Wiley & Sons, 2009).
21. G. A. Jones and D. S. Bradshaw, "Resonance energy transfer: from fundamental theory to recent applications," Front. Phys. **7**, 100 (2019).
22. J. C. Franz, S. Y. Buhmann, and A. Salam, "Discriminatory resonance energy transfer mediated by a chiral environment," New J. Phys. **26**, 053002 (2024).
23. K. A. Forbes, "Twisted light and twisted matter: the photonic frontier of chirality," Photonics Res. **14**, B193–B208 (2026).
24. K. A. Forbes, "Vortex light at the nanoscale: twists, spins, and surprises," Rep. Prog. Phys. **89**, 016401 (2026).
25. P. L. Polavarapu, *Chiroptical Spectroscopy: Fundamentals and Applications* (CRC Press, 2016).
26. L. D. Barron, *Molecular Light Scattering and Optical Activity* (Cambridge University Press, 2009).
27. K. A. Forbes, "Nonlinear chiral molecular photonics using twisted light: hyper-Rayleigh and hyper-Raman optical activity," J. Opt. **22**, 095401 (2020).
28. N. Mayer, D. Ayuso, P. Decleva, *et al.*, "Chiral topological light for detection of robust enantiosensitive observables," Nat. Photonics **18**, 1155–1160 (2024).
29. L. Cheeseman and K. A. Forbes, "Nonlinear vortex dichroism in chiral molecules," Adv. Opt. Mater. **13**, 2402151 (2025).
30. K. A. Forbes, D. Green, and G. A. Jones, "Relevance of longitudinal fields of paraxial optical vortices," J. Opt. **23**, 075401 (2021).
31. D. Green and K. A. Forbes, "Optical chirality of vortex beams at the nanoscale," Nanoscale **15**, 540–552 (2023).
32. C. S. Adams and I. G. Hughes, *Optics f2f: From Fourier to Fresnel* (Oxford University Press, 2018).
33. L. Novotny and B. Hecht, *Principles of Nano-Optics* (Cambridge University Press, 2012).
34. R. Dorn, S. Quabis, and G. Leuchs, "The focus of light—linear polarization breaks the rotational symmetry of the focal spot," J. Modern Opt. **50**, 1917–1926 (2003).

35. S. S. Stafeev, A. G. Nalimov, A. A. Kovalev, *et al.*, "Circular polarization near the tight focus of linearly polarized light," Photonics **9**, 196 (2022).
36. D. L. Andrews, "Harmonic generation in free molecules," J. Phys. B At. Mol. Phys. **13**, 4091–4099 (1980).
37. C. Tang and H. Rabin, "Selection rules for circularly polarized waves in nonlinear optics," Phys. Rev. B **3**, 4025–4034 (1971).
38. J. S. Ford and D. L. Andrews, "Molecular tensor analysis of third-harmonic scattering in liquids," J. Phys. Chem. A **122**, 563–573 (2018).
39. K. Y. Bliokh, F. J. Rodríguez-Fortuño, F. Nori, *et al.*, "Spin–orbit interactions of light," Nat. Photonics **9**, 796–808 (2015).
40. N. Berova, P. L. Polavarapu, K. Nakanishi, *et al.*, *Comprehensive Chiroptical Spectroscopy, Volume 1: Instrumentation, Methodologies, and Theoretical Simulations* (John Wiley & Sons, 2011), Vol. **1**.
41. N. Berova, P. L. Polavarapu, K. Nakanishi, *et al.*, *Comprehensive Chiroptical Spectroscopy, Volume 2: Applications in Stereochemical Analysis of Synthetic Compounds, Natural Products, and Biomolecules* (John Wiley & Sons, 2012), Vol. **2**.
42. D. L. Andrews, "Quantum formulation for nanoscale optical and material chirality: symmetry issues, space and time parity, and observables," J. Opt. **20**, 033003 (2018).
43. K. Y. Bliokh and F. Nori, "Characterizing optical chirality," Phys. Rev. A **83**, 021803 (2011).
44. R. P. Cameron, J. B. Götte, S. M. Barnett, *et al.*, "Chirality and the angular momentum of light," Philos. Trans. R. Soc. A Math. Phys. Eng. Sci. **375**, 20150433 (2017).
45. C. K. Ha, E. M. Kim, K. J. Moon, *et al.*, "Optical vortex harmonic generation enabled by confinement-induced photonic spin–orbit coupling," Nano Lett. **26**, 58–66 (2025).
46. A. K. Dharmadhikari, S. Edward, J. A. Dharmadhikari, *et al.*, "On the generation of polarization-dependent supercontinuum and third harmonic in air," J. Phys. B At. Mol. Opt. Phys. **48**, 094012 (2015).
47. E. Menshikov, P. Franceschini, K. Frizyuk, *et al.*, "Light structuring via nonlinear total angular momentum addition with flat optics," Light. Sci. Appl. **14**, 381 (2025).
48. D. P. Shelton, "Third harmonic scattering in liquids," J. Chem. Phys. **149**, 224504 (2018).
49. J. Collins, K. Rusimova, D. Hooper, *et al.*, "First observation of optical activity in hyper-rayleigh scattering," Phys. Rev. X **9**, 011024 (2019).
50. D. Verreault, K. Moreno, É. Merlet, *et al.*, "Hyper-Rayleigh scattering as a new chiroptical method: uncovering the nonlinear optical activity of aromatic oligoamide foldamers," J. Am. Chem. Soc. **142**, 257–263 (2019).
51. L. Ohnoutek, H.-H. Jeong, R. R. Jones, *et al.*, "Optical activity in third-harmonic Rayleigh scattering: a new route for measuring chirality," Laser Photonics Rev. **15**, 2100235 (2021).
52. L. Ohnoutek, J.-Y. Kim, J. Lu, *et al.*, "Third-harmonic Mie scattering from semiconductor nanohelices," Nat. Photonics **16**, 126–133 (2022).
53. D. L. Andrews, "Irreducible Cartesian tensor analysis of harmonic scattering from chiral fluids," Symmetry **12**, 1466 (2020).